Precise multi-species agricultural gas flux determined using broadband open-path dual-comb spectroscopy

Daniel I. Herman,[1,2,*] Chinthaka Weerasekara,[3] Lindsay C. Hutcherson,[4] Fabrizio R. Giorgetta,[1,2] Kevin C. Cossel,[1] Eleanor M. Waxman,[1] Gabriel M. Colacion,[1] Nathan R. Newbury,[1] Stephen M. Welch,[3] Brett D. DePaola,[4] Ian Coddington,[1] Eduardo A. Santos,[3] and Brian R. Washburn[5]

[1]National Institute of Standards and Technology, Applied Physics Division, Boulder, CO 80305

[2]University of Colorado, Boulder, Department of Physics, Boulder, CO 80309

[3]Kansas State University, Department of Agronomy, Manhattan, KS 66506

[4]Kansas State University, Department of Physics, Manhattan, KS 66506

[5]National Institute of Standards and Technology, Time and Frequency Division, Boulder, CO 80305

*daniel.herman@nist.gov

Advances in spectroscopy have the potential to significantly improve our understanding of agricultural processes and associated trace gas emissions. We implement field-deployed, open-path dual-comb spectroscopy (DCS) for precise multi-species emissions estimation from livestock. With broad atmospheric dual-comb spectra, we interrogate two paths, upwind and downwind from pens containing approximately three hundred head of cattle, providing time-resolved concentration enhancements of CH_4, NH_3, CO_2 and H_2O. We simultaneously retrieved methane and ammonia fluxes from the feedlot. The methane fluxes determined from DCS data agree to within 6% of fluxes obtained with a co-located closed-path cavity ring-down spectroscopy gas analyzer. The NH_3 concentration retrievals have sensitivity of 10 ppb and yield corresponding NH_3 fluxes with a statistical precision of 9% and low systematic uncertainty. Open-path DCS offers accurate multi-species agricultural gas flux quantification without external calibration and is easily extended to larger agricultural systems where point-sampling-based approaches are insufficient, presenting opportunities for field-scale biogeochemical studies and ecological monitoring.

In the United States, CH_4 emissions from livestock (including enteric fermentation and manure management) are thought to be the largest source of anthropogenic methane emissions (*1*), with most of these emissions attributed to

the beef and dairy industries. Precise estimation of livestock CH_4 emissions is challenging due to variability of management practices and cattle characteristics in commercial farms. Furthermore, in grazing systems, environmental drivers affect the forage quality (*2*), which, in turn, affects the enteric fermentation CH_4 emissions but remain unaccounted for in national inventories (*3*, *4*). Characterizing CH_4 flux from grazing systems is difficult as animals are unevenly distributed, limiting the efficacy of optical point sensor approaches (*5*). Cattle farms also emit considerable amounts of ammonia (NH_3), a harmful aerosol-generating pollutant (*6*). Quantification of NH_3 emissions using traditional methods is challenging due to its adsorptivity (*7–9*). Here we show that the dual-comb spectroscopy technique is capable of precisely measuring these important emissions without large systematic biases.

Open path dual-comb spectroscopy (DCS) is emerging as a powerful tool for determining greenhouse gases (GHG) emissions in the urban (*10*) and oil/gas (*11*) sectors. In DCS, the interference of two optical frequency combs generates extremely high-resolution, broadband spectra, with negligible instrument lineshape and a perfect frequency axis, while requiring no external calibration (*12–14*). Together, these properties improve the analysis of overlapping spectral features that appear in broadband atmospheric spectra and allow DCS to provide accurate path-averaged multi-species concentrations and temperature measurements (*15*). Additionally, the high brightness and spatial coherence of comb sources enables precise spectroscopic measurements over kilometer scale paths. The precision achievable by DCS will lead to less uncertainty on livestock methane emission rates, thus improving the overall uncertainty of national-level enteric fermentation models (*16–18*).

In this Article, we demonstrate DCS for multi-species (CH_4, NH_3, CO_2 and H_2O) quantification of gas emission flux from a small beef cattle feedlot and simultaneously validate the DCS system against a closed-path cavity ring-down spectroscopy (CRDS) gas analyzer. Measurements were performed between October 2019 to January 2020 and yielded over 10 days of CH_4 flux data for a field comparison of the two techniques. Fluxes are determined using an inverse Lagrangian dispersion model (IDM) that combines meteorological data with upwind and downwind concentrations from both the DCS and CRDS, and methane fluxes from both systems agree to within model error. Our experimental design enables reliable benchmarking against a standard technique, however, the open-path DCS should allow for precise flux estimation in much larger pasture systems with sparser point sources. Additionally, NH_3 emission rates from the feedlot are also determined using DCS with statistical precision of <10%, highlighting the versatility of broadband open-path laser spectroscopy for agricultural sensing.

Dual-Comb System

The open-path DCS system (Fig. 1A) covers 35 THz from 1.4 μm to 1.7 μm with fully coherent frequency combs that can resolve the atmospheric transmission across over 175,000 individual comb teeth. The system is designed to target multiple gas species with laboratory-level precision while operating in the field conditions of a cattle feedlot (Fig. 1, B and C). It is based on all-polarization-maintaining, SESAM-modelocked erbium-doped fiber lasers with repetition rates near 200 MHz. Mutual comb coherence is established by phase locking each comb to the same free-running 1560 nm external-cavity diode laser (ECDL) and by phase locking the carrier-envelope offset frequency (f_0) of each comb using an in-line *f*-to-2*f* interferometer (*19*). Additionally, excess phase noise on the locks was subtracted in real time from the DCS interferogram signal using a field-programmable gate array (FPGA) (*20*, *21*). The repetition rate difference (rate of interferograms recorded per second) was set to 208 Hz. To tailor the comb spectrum, light for each comb was amplified to ~1 nJ per pulse in an erbium-doped fiber amplifier and sent through a short (~3 cm) piece of highly nonlinear fiber (HNLF). The 35-THz wide spectra were filtered with 25 nm wide band-stop fiber-coupled micro-optic filters centered near 1560 nm to block light without useful molecular absorption, maximizing achievable signal-to-noise ratio (SNR). The final DCS spectrum covered absorption features from CH_4, CO_2, NH_3 and H_2O (Fig. 2, A to D). For the DCS measurement, the filtered outputs were combined using a 50:50 fiber combiner generating two outputs that were directed over two open-air paths (Fig. 1A). Our DCS derives its concentration accuracy from HITRAN-based (*22*, *23*) fitting routines and its wavelength accuracy from a GPS-disciplined quartz oscillator(*19*). There is no need for field calibration.

Measurement Geometry

This work was performed at a Kansas State University beef cattle research unit outside of Manhattan, Kansas (Fig. 1, B and C). The 288 heads of cattle at the site were contained in a pen measuring 70 m (north to south) by 60 m (east to west). Lasting from late October 2019 to early January 2020, the measurement captured gaseous emissions from both the cattle themselves (*i.e.* CH_4 from enteric fermentation) as well as area-distributed emissions (*i.e.* CH_4 and NH_3 from manure management). The DCS measured two paths, north and south of the cattle pen, allowing both an upwind measurement (background) and a downwind measurement (enhancement). In the Manhattan area, prevailing winds from autumn to winter are northerly and southerly (fig. S1A). Temperatures at the site varied widely from -10 °C to 20 °C (fig. S1B). The site is surrounded by open, ungrazed pasture on all sides, providing stable background concentrations with values close to typical atmospheric background levels (*5*, *24*, *25*).

The DCS system was housed in a trailer parked on the feedlot's north side. A 10-meter-long single-mode fiber (SMF) connected the first dual-comb output to the north telescope. The simple telescopes each consist of an APC fiber termination followed by a collimating 179 mm focal length, 102 mm diameter, 45° off-axis parabolic mirror. About 10 mW of eye-safe collimated dual-comb light was directed at a 5 cm diameter retroreflector positioned 50 m away and the reflected signal was recoupled back into the launch fiber with about 25% efficiency. The returned dual-comb light was attenuated to ≤200 μW and coupled onto a 150-MHz bandwidth InGaAs photodiode. A significant advantage of near-infrared (NIR) DCS is the ability to use fiber to probe open-air paths far from the comb sources. To reach the south path the dual-comb light was transported both ways through a 200 m long duplexed SMF. Both telescopes were mounted on automatic gimbals that were re-aligned remotely using co-aligned silicon CCD cameras. Each open-air path has slight height variations along its 50-m distance, ranging from 1.5 m to 2.0 m above ground, which is included in the flux-estimation model described in the Materials and Methods section.

For each path the InGaAs photodiode signal was low-pass filtered at 100 MHz and then digitized and phase-corrected in real time on an FPGA (*20*, *21*). In addition to these two DCS signals, inputs to the FPGA include the four phase-locked frequencies for stabilizing the two combs (*i.e*. the two optical beat notes and two carrier-envelope offset frequencies), the two comb repetition rates, and an external 10 MHz clock. The real-time correction algorithm removes both phase and timing jitter in the interferograms and co-adds them to yield a single spectrum every 5 minutes. In addition, a 3D sonic anemometer was positioned on a tower near the north path at approximately 3.5 m above the ground to record wind information every 100 ms.

Results

DCS Spectra and Methane Concentration Retrievals

The DCS spectrum acquired at the feedlot over the standard 5-minute integration time resolves hundreds of narrow absorption features over its 35 THz bandwidth, the broadest spectrum ever captured using atmospheric open-path DCS (Fig. 2A). The absorption from CH_4, CO_2 and H_2O below 190 THz is weak for these short 100-m round-trip optical path lengths, but one can observe the small percent-level absorption lines in zoomed-in spectra (Fig. 2, B and C). This small absorption provides enough signal to retrieve reliable concentrations with DCS. Above 198 THz, the water absorption becomes stronger and visible in the unexpanded spectrum. Underneath this strong water absorption are

multiple weak NH_3 absorption features (Fig. 2D). Our ability to retrieve NH_3 concentrations amid this forest of strong water lines is evidence of the benefits of the bandwidth, resolution and low spectral distortion possible with DCS. The total spectrum consists of over 175,000 spectral elements at 200 MHz point spacing (*i.e.* over 35 THz of optical bandwidth). The DCS figure-of-merit (FOM), defined as the product of the SNR and number of spectral elements, is in excess of 1.5×10^7 for a 5 minute average, comparable to laboratory-based DCS systems (*12*).

Clear enhancements are visible in the time series of measured CH_4 concentrations from the DCS and CRDS systems for over 8 hours on the night of November 17th, 2019 (Fig. 3A). Similar concentration time series are retrieved for NH_3 as discussed below and for H_2O and CO_2 as shown in the Supplementary Materials (fig. S2, A and B). Methane concentrations are averaged to 15 minute time resolution, the minimum time over which our flux calculation is taken to be valid (*8*, *26–28*). Typically, CH_4 downwind enhancements with cattle present were 600 ppb above the ~2 ppm background but could exceed 1 ppm during less windy periods. CH_4 concentrations from the two sensors and both paths compare well within the 25 ppb DCS experimental measurement precision estimated from the Allan-Werle deviations (*29*) of the upwind data (Fig. 3B). Allan-Werle deviations generalize the notion of measurement instability with each point signifying the measurement instability over a given averaging period. The CH_4 DCS precision at 900 seconds is 1.25 ppm·m (path-averaged concentration precision of 25 ppb), which matches the 1 ppm·m to 3 ppm·m precision reported previously (*15*). Using the same method, the CRDS precision at 900 seconds was estimated to be ~2 ppb. An upwards slope visible on the CRDS upwind Allan-Werle deviation (Fig. 3B) is driven by background methane variability.

By this measure, the CRDS is an order of magnitude more precise than the DCS on the background (upwind) channel. However, this higher instrument precision ignores the added sampling uncertainty associated with intermittent point sensing compared to continuous open-path sensing. The strength of DCS is seen in the downwind channel, where DCS provides a more precise measure of gas concentration than CRDS (Fig. 3B) despite having higher instrument uncertainty. With only four gas inlets along each path and less than 50% uptime on either path for one 5-minute measurement cycle, the CRDS is more susceptible to stochastic CH_4 plume variability than is the path-averaged and continuous dual-channel DCS sensor. In this experiment, the benefit in precision provided by continuous and path-averaged sampling is as large as 20 ppb to 40 ppb (calculated as the difference in Allan-Werle deviations at 900 seconds for downwind DCS and CRDS), comparable to the background statistical precision of the DCS sensor of 25 ppb. In this experiment, the homogeneous feedlot source provided a near ideal plume geometry for emissions

quantification and yet the point sensor system still had decreased downwind precision due to insufficient temporal and spatial sampling. In a pasture system, where multiple, dispersed point sources create non-uniform plumes, a continuous integrated-path measurement will provide much larger improvements in precision over a multiport sampling system connected to a point sensor.

Methane Flux

We examine an 11-hour period during the night of November 24th, 2019 with appropriate weather conditions for flux retrievals with our IDM (see Materials and Methods) and complete coverage by both the DCS and CRDS systems (Fig. 4, A to E). The CH_4 concentrations are given for both the upwind and downwind paths from both the DCS and CRDS systems (Fig. 4B). In addition, the CH_4 flux from both the DCS and CRDS data are shown with the CH_4 flux from the feedlot showing clear time dependence on the hour timescale (Fig. 4, C and F). These changes are easily quantifiable with the 5-minute resolution of our sensors and the averaged 15-minute resolution of the flux calculation. The DCS and CRDS measurements yield similar time dependent methane fluxes from the feedlot with values ranging from 100 μg/m^2/s to 200 μg/m^2/s. The methane flux does show some disagreement during a period of small enhancement after 2:00 a.m. when winds were fast and near the edge of acceptable directions (Fig. 4C).

To compare the flux retrieved from the DCS and CRDS, we examine the correlation between values measured simultaneously with both sensors throughout the 4-month measurement campaign (Fig. 5). We fit a linear slope to this correlation by splitting the data into two groups: days with cattle present (Day 305 to Day 346) and days without cattle (Day 347 to Day 355). Even without cattle present, there is a baseline level of methanogenic bacterial activity in the feedlot manure, leading to methane flux values with an average of 18±11 μg/m^2/s. The intercept of the linear regression of the days without cattle (*i.e.* small flux measurements) is used as the intercept for a linear fit to the entire flux dataset. The intercept is calculated to be 1.8 μg/m^2/s (2% of typical CH_4 flux) and the slope is found to be 1.06, signifying a 6% bias between DCS and CRDS flux estimates. This close agreement between DCS and CRDS flux values was achieved without calibration of the DCS instrument as is required for continuous-wave (CW) laser sensors measuring comparable path-integrated concentrations (~100 ppm·m) (*30*). The demonstrated ability of DCS to measure methane flux accurately without intensive calibration and on multiple remote fiber-connected paths enables wider deployment of DCS systems for methane emissions inventory development and mitigation efforts.

Ammonia Concentrations and Flux

The same DCS instrument that allows for accurate, calibration-free quantification of feedlot methane emissions simultaneously provides precise time-resolved ammonia concentrations upwind and downwind of the feedlot (Fig. 4D). The average NH_3 background concentration was 60 ppb, equivalent to background feedlot NH_3 levels reported in the literature(*24*) but above standard atmospheric levels of 4 ppb (*25*). This elevated background is likely due to the proximity of the open-path sensors to the emission area. The average NH_3 enhancement was 430 ppb over background with some enhancements up to 1 ppm. An Allan-Werle deviation of the ammonia background gives a precision of about ~10 ppb or 0.5 ppm·m at 900 second averaging time. Interestingly, the first demonstration of open-path DCS captured NH_3 absorption signatures with a beam passing over an open bottle of ammonia (*31*). We return to these roots by demonstrating the first coherent, high resolution, open-path DCS detection of NH_3 which enables quantification of feedlot NH_3 flux with precision rivaling commercial sensors (*8*, *32*) while also providing vital CH_4 flux.

Using the same IDM as for CH_4, NH_3 fluxes were calculated at 15-minute intervals (Fig. 4E). The fractional uncertainty in NH_3 flux measurement due to DCS instrument error alone is 3.5% for the average enhancement of 430 ppb (see Materials and Methods). The Allan-Werle deviation can also be applied directly to flux time series and results in a statistical precision at 900 seconds of 8 $\mu g/m^2/s$ (8% of average NH_3 flux). This analysis of instrument precision ignores potential biases from baseline distortion, detector nonlinearity and crosstalk in the spectral model used to fit NH_3 and neighboring H_2O absorption features centered at 1510 nm (Fig. 2D). The uncertainty due to crosstalk is estimated at <5% (see Supplementary Materials). Detector nonlinearity was not a large issue in this experiment as the received light was highly attenuated and no deep absorption lines were used in the analysis. The cepstral-domain fitting technique implemented in this work (see Materials and Methods) has been shown to be less sensitive to baseline fluctuations (*33*). Still, some bias in ammonia concentration due to the choice of cepstral-domain filter function remains at a level comparable to the reported statistical precision (<5%). The combined uncertainty due to the effects discussed here is <10%, smaller than the ~20% disagreement found in previous comparisons of ammonia flux estimation methods (*8*, *9*).

Diurnal Cycles of Methane and Ammonia

The gas emission rate from the feedlot (and from agricultural systems in general) fluctuates over time and thus continuous measurement over a variety of conditions is necessary for complete understanding of these emission sources. Diurnal cycles for both methane and ammonia fluxes from the feedlot were generated by binning individual

15-minute flux averages by hour of day for days when cattle were present (Fig. 4, F and G). In total, dual-comb spectroscopy (DCS) data from 12 days is included in the diurnal cycle analysis which amounted to 341 DCS flux calculations or an average of 14 DCS flux measurements per bin. A DCS flux average is only shown when the hour bin contains three or more 15-minute averages (Fig. 4, F and G). The diurnal cycles with cattle present measured by DCS and cavity ring-down spectroscopy (CRDS) match within statistical error bars. The morning hours are not as well covered by the DCS system as rapid temperature shifts and frosting on optical components made telescope alignment more challenging. Ruggedized telescopes developed for DCS oil and gas research will be incorporated in the future to mitigate this issue (*34*). The DCS itself operated robustly for the duration of the field campaign, breaking phase locks only a handful of times over the three months in the field.

A clear diurnal cycle in CH_4 production from the feedlot is observed with increased CH_4 fluxes during daylight hours (Fig. 4F). An increase in CH_4 appears after morning and afternoon feeding times (6 a.m. to 7 a.m. and 1 p.m. to 2 p.m.) suggesting that the source of the CH_4 emissions originates from increased cattle digestion and associated enteric fermentation (*4*, *35*). No such trend is seen in hourly-binned data when the cattle were not present although microbial activity in the manure still produces a small methane flux. The nighttime CH_4 flux stabilizes as the cattle sleep and the rate of enteric fermentation slows down considerably. The average DCS CH_4 flux during the presence of cattle (155±85 $\mu g/m^2/s$) minus the manure contribution (18±11 $\mu g/m^2/s$) gives an average cattle CH_4 flux of 137±86 $\mu g/m^2/s$. This number compares well with the IPCC 2006 (*18*) guideline number for beef cattle CH_4 emissions normalized to our feedlot size (~135 $\mu g/m^2/s$), although every agricultural system is slightly different and deviations from this value are to be expected depending on cattle feed and manure management techniques.

For time periods with good data coverage (all times but 9 am to 12 pm), the diurnal cycle for NH_3 (Fig. 4G) shows less variation than that of CH_4. The NH_3 diurnal cycle shows a more constant daily flux with an average of 104±39 $\mu g/m^2/s$ or 116 grams per head per day. This average compares well to literature values from measurements conducted in the central U.S. at concentrated dairy/beef cattle feeding operations during similar times of the year (*36*–*38*). For instance, the mean per capita emission rates of NH_3 during Autumn months at two Texas panhandle beef cattle feedyards were 122 grams per head per day and 83 grams per head per day, measured using a single open-path continuous-wave (CW) laser sensor. The overall range of NH_3 emission rates from the same feedyards varied between 31 grams per head per day in January to 207 grams per head per day in October (*37*). All the NH_3 fluxes measured with cattle present at our Kansas test site fall within this range of values (Fig. 6A). NH_3 does not originate from

digestive processes, rather it originates from hydrolysis of urea in the manure deposited on the ground in the feedlot pens and the emission rate fluctuates slightly over the course of the day, which has been observed in other feedlots as well (*39*). The lack of a clear pattern is attributed to the many factors that must be considered when studying the rate of hydrolysis of urea and subsequent volatilization of gaseous NH_3. It is known that temperature, soil water content, soil pH and wind conditions can all modulate the rate of NH_3 release from agricultural soils (*40*). It is also known that differences in the variety of bacteria in soil can alter the dependences of any given soil ecosystem to the environmental factors (*41*).

Ammonia Flux Dependence on Temperature and Wind

Our open-path DCS measurement reveals the dependence of NH_3 flux on temperature and wind speed (Fig. 6). Assuming constant pH, soil temperature, total ammoniacal N in solution and mass transport coefficient, the volatilization of ammonia should generally follow a functional form proportional to Henry's volatility constant (K_h) for ammonia-water solution at a given temperature (*40*, *42*). This form can be expressed(*40*) as $K_h = (A/T)10^{6.123-1825/T}$, where A is a proportionality coefficient and T is the ambient air temperature in K. A fit to this function is applied to the estimated NH_3 fluxes with an R^2 value of 0.36 (Fig. 6A), although it should be noted that a linear fit of the data provides a similar R^2 value. Importantly, the fit conveys the general increase in volatilization as a function of ambient air temperature which has been demonstrated previously (*43*, *44*). Factors such as microbial activity (*41*), manure pH (*40*), freeze-thaw-cycles (*45*) and winds (*40*) contribute to large deviations from the Henry model. Microbial activity and manure pH were not measured but can reasonably be taken to vary on seasonal timescales (*43*). Evidence of complicated freeze-thaw dynamics is apparent in our single season dataset, with a large spread of reported flux estimates in the 0 ˚C to 5 ˚C range, just above the freezing point of water. For fixed temperatures above the freezing point and fixed surface characteristic lengths, modeling shows (*40*) that volatilization scales nearly linearly with average wind speed, U. For temperatures above 7 ˚C, a power law, $F = AU^B$, can be reliably fit (R^2 = 0.65) to the NH_3 flux data (Fig. 6B) yielding B = 0.77. This result falls very close to the literature value (*40*) of 0.8, good evidence of wind-dependent emission rates of NH_3 from the feedlot. The large dependence of ammonia volatilization on environmental parameters stresses the importance of extended continuous field measurements such as those provided by calibration-free open-path DCS. For example, our results on the wind dependence of ammonia emission rate will inform future studies aimed at reducing ammonia emissions using modern management practices such as restricted grazing (*46*), targeted manure application (*47*) and agricultural windbreaks (*48*).

Discussion

In this work, we demonstrate the advantages of broadband, high resolution laser sensing by using coherent, open-path DCS for agricultural gas flux quantification for the first time at a small beef cattle feedlot. The large DCS bandwidth covered absorption from four different molecular species: CH_4, NH_3, CO_2 and H_2O. We specifically target the CH_4 and NH_3 emissions, which are the most important for this agricultural system. DCS simultaneously achieves sub-ppm·m detection sensitivity for NH_3 and ppm·m-level sensitivity for CH_4. Note that without the high resolution offered by our fully coherent technique, broadband sensing for NH_3 in this convenient band (located next to the useful telecom C-band) would be next to impossible due to H_2O clutter (Fig. 2D). Furthermore, the DCS is configured to measure across two displaced open-air paths using fiber-coupled telescopes. In this way, we continuously monitor the concentration over widely separated upwind and downwind open paths, which then allows for accurate flux estimation based on the directly observed concentration enhancement. We find the open-path configuration of the DCS captures downwind enhancements due to the gas emission with higher precision than a standard closed-path technique for certain wind conditions. When input to an IDM model, the upwind/downwind DCS data yield a methane flux for the cattle feedlot that agrees to within 6% of the flux estimated by a co-located closed-path CRDS system, which is well within the 10% uncertainty attributed to flux models of this type (*28*). This agreement against a standard agricultural measurement technique gives us confidence that DCS accurately quantifies gas flux in an agricultural context. Due to the length of tubing required to transverse the feedlot site, a double path measurement of ammonia using CRDS cannot easily provide a reliable benchmark. Yet, the retrieved NH_3 flux estimate from the DCS data generally agree with the literature in terms of absolute magnitude and dependence on environmental parameters (Fig. 6).

A major motivation for this work is that the DCS system can be extended to estimate emissions from much larger areas. To this end, we briefly consider the requirements for estimating CH_4 flux from a 500 m by 500 m pasture containing 40 cattle. When our values are scaled to 500 m paths, the achievable DCS precision at 900 seconds should be around 2 ppb, in line with previous NIR DCS demonstrations (*15*). Assuming a standard box model for the cattle emissions (*49*), we can scale the average CH_4 enhancement ($E = C_{sig} - C_{bkg}$) measured in our feedlot to a possible pasture enhancement (E') using the following relation:

$$E' = E\frac{wN'}{w'N}. \quad (1)$$

Note w is the feedlot width (60 m), w' is the pasture width (500 m), N is the number of cattle in the feedlot (288 head) and N' is the number of cattle in the pasture (40 head). Equation (1) assumes that w' is less than the average horizontal wind speed times the measurement integration period, which assumption should be satisfied for w' = 500 m and a 15-minute integration time. Using equation (1), the enhancement on the downwind edge of the 500 m by 500 m would be on average around 10 ppb. By averaging fluxes rather than concentrations, this enhancement will yield a methane flux uncertainty of 10% after ~2.25 hours. For GHG inventories one would like to measure weekly or monthly averaged emission with >10% flux uncertainty (*3*, *17*), which is easily supported at this time resolution. Subdividing the pasture with additional beam paths could greatly reduce averaging times if higher time resolution is required.

Looking towards the future, the open-path advantage of DCS motivates future pasture-scale flux estimation. As discussed above, the same approach used here should be applicable to methane and ammonia emissions from larger areas and will improve efforts to accurately quantify livestock and other agricultural contributions to GHG inventories. Open-path alternatives to standard techniques are especially advantageous for NH_3 detection given that the 'sticky', reactive nature of NH_3 demands difficult calibration of extractive NH_3 analyzers. Here we have shown that DCS is a viable solution for sub-ppb level sensing of NH_3 over kilometer scales in a system that simultaneously provides information about multiple other gaseous species with precision comparable to single-species open-path sensors (*8*, *50*, *51*). The DCS NH_3 sensing has already provided useful in-situ data regarding the wind dependence of ammonia volatilization rates, simultaneously benchmarking biogeochemical models and encouraging further emissions mitigation research (*40*, *47*). In the future, multi-species DCS sensing will help determine accurate environmental dependences of CH_4-NH_3 and CO_2-NH_3 emission factor ratios, ultimately improving our understanding of microbial activity and carbon exchange in feedlot and grassland ecosystems (*43*, *52*). While the current system operated in the NIR, continued advances of DCS further into the mid-infrared provides opportunities for the flux quantification of a greater number of gases and with greater sensitivity. In particular, the 2.0 μm to 2.4 μm spectral band presents increased sensitivity to CO_2, CH_4, and NH_3, and is accessed using photonic waveguides (*53*, *54*). Additionally, many groups have recently demonstrated advances in mid-infrared DCS sensing (*55–61*). The functional group region (3 μm to 5 μm) includes atmospheric transmission windows with access to strong CH_4, CO_2 and N_2O absorption. Precision N_2O emissions measurements are particularly interesting for the atmospheric sensing community as N_2O remains an understudied portion of global agricultural GHG emissions and a threat to the stratospheric O_3 layer (*62*).

Field-scale DCS flux measurements covering multiple nitrogen-containing species (*i.e.* NH_3 and N_2O) will enable improved benchmarking of soil biogeochemical models (*63*). The mid-infrared can also be used for sensing of biogenic volatile organic compounds (BVOC) and O_3, enabling advanced monitoring of plant health and agricultural aerosol production (*64*). As part of the larger vision of "precision agriculture," the frequency comb offers precise gas fluxes for many species simultaneously over large spatial scales which will one day enable sustainable and more productive farming.

Materials and Methods

CRDS Setup

The DCS approach was also validated against a more traditional CRDS measurement of CH_4, CO_2 and H_2O performed using a commercial trace gas analyzer (G2311-f, Picarro) which was housed in the same trailer as the DCS system. Prior to the field deployment, the CRDS analyzer underwent a multi-point calibration using primary CH_4 and CO_2 World Meteorological Organization (WMO) calibration standards (Global Monitoring Laboratory, NOAA, Boulder). At the measurement site, the CRDS analyzer was connected to a custom-built gas manifold. Four air inlets were deployed at the north edge of the feedlot and another four air intakes were set up at the south edge of the feedlot. Each air intake consisted of a 1 m stainless steel tube (0.43 cm inner diameter) with a rain diverter and mesh screen in one of its extremities. The other extremity of the tube was connected to a stainless-steel filter (7 μm sintered element filter). In order to prevent condensation, the filter holder was heated using a 0.5 W heater connected to a 12 V DC power supply and a critical flow orifice located downstream of the filter was used to reduce the air pressure in the intake line and to ensure similar flow rate at all intakes. A polyethylene/aluminum tube (0.43 cm inner diameter) draws air from the intakes to the custom-made manifold.

The manifold was used to control the air flow from air intakes to the CRDS gas analyzer. The manifold switched between north and south air intakes every 30 seconds. The air was drawn continuously through all air intakes at a flow rate of approximately 1900 $cm^3\ min^{-1}$ using a diaphragm vacuum pump. A sample of the total flow was directed to the CRDS analyzer at a flow rate of 300 $cm^3\ min^{-1}$. All gas transported to the CRDS sample cell is heated to 60 ˚C before measurement and the CRDS only reports concentrations when its cell temperature is stable. Certified calibration tanks were used to verify the CRDS measurements every six hours. Concentrations measured by the CRDS gas analyzer were recorded at a rate of 10 Hz and north and south paths data were averaged every 30s. The first 15 s of

data after switching intakes is discarded to ensure the flushing of the sampling line is not included in the averaged measurement period.

Micro-meteorological Techniques and Flux Modeling

Gas emission flux is determined using an IDM (*27*) using the measured upwind and downwind concentrations combined with appropriate wind statistics as inputs. IDM is a well-established micro-meteorological method to determine scalar exchange from well-defined source areas. This model is particularly adept at quantifying gas emissions from source areas with well-defined boundaries. The IDM uses the rise of concentration downwind from the source and wind statistics to determine the source emission rate. Numerous validation studies have been conducted under field conditions by releasing a tracer gas at known flow rate and estimating the recovery rate with the IDM (*27*, *28*, *65–67*). These studies have reported an emission rate accuracy of ±10%. A freely available IDM software, WindTrax (*27*), was used for these dispersion simulations.

The IDM approach requires appropriate weather conditions to calculate reliable gas flux results and data was filtered based on the following criteria. As WindTrax is only valid on 15 minute or longer timescales, we averaged the 5 minute raw concentration data to 15 minutes (900 seconds) (*8*, *27*). For our beam layout, wind direction (θ) was required to be northerly or southerly ($315^\circ < \theta < 45^\circ$ or $135^\circ < \theta < 225^\circ$). Acceptance criteria for friction velocity (u^*) and Monin-Obukhov Length (L) were set at $u^* > 0.1$ m/s and $|L| > 10$ m/s (*68*). The weather statistics at the site satisfied these criteria 60% of the total measurement time. The site wind conditions, temperature and precipitation records are available for all measurements (fig. S1). The gas emission region (Fig. 2B) used by the IDM included only the cattle pens consisting of an area of 3731 m^2 (the road in between the pens was not included in the emission region). In WindTrax both the DCS and CRDS north/south path concentration measurements were modeled as line concentration sensors with 30 points, starting at the telescope and ending at the retroreflector.

One of the principal sources of uncertainty in the IDM arises from the uncertainty in the concentration measurements themselves, either from the DCS instrument or CRDS instrument. The resulting fractional uncertainty in the flux can be estimated from the following:

$$\frac{\sigma_F}{F} \sim \frac{\sqrt{2}\sigma_{C,bkg}}{C_{sig} - C_{bkg}}, \quad (2)$$

where F is flux, σ_F is flux uncertainty, $\sigma_{C,\,bkg}$ is background concentration uncertainty, C_{sig} is signal (downwind) concentration and C_{bkg} is the background (upwind) concentration. This formula assumes equal precision on background and signal paths and ignores errors due to measurement deadtime and geometry as well as uncertainty in wind field measurements and inherent model uncertainty. Equation (2) is designed to capture the instrument contribution to measurement uncertainty. The average CH_4 enhancement (absolute value of the concentration difference between paths) measured by the CRDS and DCS over the course of the measurement campaign was approximately 600 ppb. Combining this average enhancement with our DCS precision of 25 ppb yields an average normalized DCS flux uncertainty of 6% using equation (2). For further comparison of CH_4 concentration measurements using DCS and CRDS, see the Supplementary Materials (fig. S3).

Concentration Retrieval using Cepstral Analysis

The spectra are analyzed using a fit model derived from a combination of the HITRAN 2008 and 2016 databases and the cepstral-domain technique (*22*, *23*, *33*). HITRAN 2008 was used for all molecules except NH_3 for comparison with previous NIR DCS results. The dual-comb spectra are chopped into three bands: 1, 2 and 3, respectively covering 179.3 THz to 184.3 THz, 197.2 THz to 200.7 THz and 185.7 THz to 187.4 THz. These bands are used to retrieve CH_4, CO_2 and NH_3/H_2O respectively (Fig. 2A). Temperature and pressure data for the fit model are provided by a sonic anemometer (*69*, *70*) and a weather station, respectively, which were both located on the same tower during the measurement campaign (Fig. 2B). The bias associated with fixing the temperature to this external value has a statistically negligible effect on methane and ammonia emission rates (see the Supplementary Materials). Band 1 contains CH_4, as well as weak carbon dioxide and water absorption features that are fixed by the fits from bands 2 and 3, respectively. The CH_4 model (HITRAN 2008) contains 108 features with line-strength (S) > 10^{-22} $cm^{-1}/(molecule \times cm^{-2})$. A cepstral-domain filter (lifter) (*33*) which mimics a high-pass filter in the frequency domain removes comb baseline structure broader than ~100 GHz for band 1. Band 2 contains both CO_2 and weak H_2O absorption. 36 CO_2 features from HITRAN 2008 with $S > 10^{-24}$ $cm^{-1}/(molecule \times cm^{-2})$ are included in the fit model. The H_2O concentration is held fixed at its value retrieved from band 3. A 40-GHz cepstral filter is used for band 2. Band 3 is fit to retrieve both H_2O and NH_3 concentrations. Fits in band 3 must deal with a large amount of spectral interference between species (Fig. 2D). In all, 82 H_2O features with $S > 10^{-24}$ $cm^{-1}/(molecule \times cm^{-2})$ and 39 NH_3 features with $S > 10^{-21}$ $cm^{-1}/(molecule \times cm^{-2})$ are included in the model for Band 3. A 70-GHz cepstral filter is used for band 3. The filters are chosen by examining the structure of the cepstral fit residuals and are held constant for all

analyses. Etalons are easily filtered out in the cepstral domain by adding notches to the cepstral filters to remove data points near the etalon appearance time (*33*). Strong H_2O absorption and overlapping weak CO_2 absorption are also measured below 1490 nm but are not analyzed in this work due to challenges associated with fitting deep absorption features. All reported DCS and CRDS concentrations are the dry values with the water concentration fixed to the value from each respective sensor.

References

1. U.S. Environmental Protection Agency, Inventory of U.S. Greenhouse Gas Emissions and Sinks: 1990-2018. *EPA430-R-20-002* (2020) (available at https://www.epa.gov/ghgemissions/inventory-us-greenhouse-gas-emissions-and-sinks-1990-2018).

2. A. Mosier, D. Schimel, D. Valentine, K. Bronson, W. Parton, Methane and nitrous oxide fluxes in native, fertilized and cultivated grasslands. *Nature*. **350**, 330–332 (1991).

3. U.S. Environmental Protection Agency, Annexes to the Inventory of U.S. GHG Emissions and Sinks 1990-2018 (2020) (available at https://www.epa.gov/ghgemissions/inventory-us-greenhouse-gas-emissions-and-sinks-1990-2018).

4. R. Todd, C. Moffet, J. Neel, K. Turner, J. Steiner, A. Cole, Enteric Methane Emissions of Beef Cows Grazing Tallgrass Prairie Pasture on the Southern Great Plains. *Trans. ASABE*. **62**, 1455–1465 (2019).

5. T. K. Flesch, J. A. Basarab, V. S. Baron, J. D. Wilson, N. Hu, N. W. Tomkins, A. J. Ohama, Methane emissions from cattle grazing under diverse conditions: An examination of field configurations appropriate for line-averaging sensors. *Agric. For. Meteorol.* **258**, 8–17 (2018).

6. S. E. Bauer, K. Tsigaridis, R. Miller, Significant atmospheric aerosol pollution caused by world food cultivation. *Geophys. Res. Lett.* **43**, 5394–5400 (2016).

7. D. J. Miller, K. Sun, L. Tao, M. A. Khan, M. A. Zondlo, Open-path, quantum cascade-laser-based sensor for high-resolution atmospheric ammonia measurements. *Atmospheric Meas. Tech.* **7**, 81–93 (2014).

8. H. Baldé, A. VanderZaag, W. Smith, R. L. Desjardins, Ammonia Emissions Measured Using Two Different GasFinder Open-Path Lasers. *Atmosphere*. **10**, 261 (2019).

9. K. von Bobrutzki, C. F. Braban, D. Famulari, S. K. Jones, T. Blackall, T. E. L. Smith, M. Blom, H. Coe, M. Gallagher, M. Ghalaieny, M. R. McGillen, C. J. Percival, J. D. Whitehead, R. Ellis, J. Murphy, A. Mohacsi, A. Pogany, H. Junninen, S. Rantanen, M. A. Sutton, E. Nemitz, Field inter-comparison of eleven atmospheric ammonia measurement techniques. *Atmospheric Meas. Tech.* **3**, 91–112 (2010).

10. E. M. Waxman, K. C. Cossel, F. Giorgetta, G.-W. Truong, W. C. Swann, I. Coddington, N. R. Newbury, Estimating vehicle carbon dioxide emissions from Boulder, Colorado, using horizontal path-integrated column measurements. *Atmospheric Chem. Phys.* **19**, 4177–4192 (2019).

11. S. Coburn, C. B. Alden, R. Wright, K. Cossel, E. Baumann, G.-W. Truong, F. Giorgetta, C. Sweeney, N. R. Newbury, K. Prasad, I. Coddington, G. B. Rieker, Regional trace-gas source attribution using a field-deployed dual frequency comb spectrometer. *Optica*. **5**, 320–327 (2018).

12. I. Coddington, N. Newbury, W. Swann, Dual-comb spectroscopy. *Optica*. **3**, 414–426 (2016).

13. N. Picqué, T. W. Hänsch, Frequency comb spectroscopy. *Nat. Photonics*. **13**, 146–157 (2019).

14. G. B. Rieker, F. R. Giorgetta, W. C. Swann, J. Kofler, A. M. Zolot, L. C. Sinclair, E. Baumann, C. Cromer, G. Petron, C. Sweeney, P. P. Tans, I. Coddington, N. R. Newbury, Frequency-comb-based remote sensing of greenhouse gases over kilometer air paths. *Optica*. **1**, 290–298 (2014).

15. E. M. Waxman, K. C. Cossel, G.-W. Truong, F. R. Giorgetta, W. C. Swann, S. Coburn, R. J. Wright, G. B. Rieker, I. Coddington, N. R. Newbury, Intercomparison of open-path trace gas measurements with two dual-frequency-comb spectrometers. *Atmospheric Meas. Tech.* **10**, 3295–3311 (2017).

16. J. Mangino, K. Peterson, H. Jacobs, in *12th International Emission Inventory Conference - "Emission Inventories - Applying New Technologies"* (San Diego, California, USA, 2003; https://www3.epa.gov/ttn/chief/conference/ei12/green/mangino.pdf).

17. Committee on Anthropogenic Methane Emissions in the United States: Improving Measurement, Monitoring, Presentation of Results, and Development of Inventories, Board on Atmospheric Sciences and Climate, Board on Agriculture and Natural Resources, Board on Earth Sciences and Resources, Board on Energy and Environmental Systems, Board on Environmental Studies and Toxicology, Division on Earth and Life Studies, National Academies of Sciences, Engineering, and Medicine, *Improving Characterization of Anthropogenic Methane Emissions in the United States* (National Academies Press, Washington, D.C., 2018; https://www.nap.edu/catalog/24987).

18. In *2006 IPCC Guidelines for National Greenhouse Gas Inventories* (Institute for Global Environmental Strategies, 2006; https://www.ipcc-nggip.iges.or.jp/public/2006gl/index.html), vol. 4.

19. G.-W. Truong, E. M. Waxman, K. C. Cossel, E. Baumann, A. Klose, F. R. Giorgetta, W. C. Swann, N. R. Newbury, I. Coddington, Accurate frequency referencing for fieldable dual-comb spectroscopy. *Opt. Express*. **24**, 30495–30504 (2016).

20. J.-D. Deschênes, P. Giaccarri, J. Genest, Optical referencing technique with CW lasers as intermediate oscillators for continuous full delay range frequency comb interferometry. *Opt. Express*. **18**, 23358–23370 (2010).

21. J. Roy, J.-D. Deschênes, S. Potvin, J. Genest, Continuous real-time correction and averaging for frequency comb interferometry. *Opt. Express*. **20**, 21932–21939 (2012).

22. I. E. Gordon, L. S. Rothman, C. Hill, R. V. Kochanov, Y. Tan, P. F. Bernath, M. Birk, V. Boudon, A. Campargue, K. V. Chance, B. J. Drouin, J.-M. Flaud, R. R. Gamache, J. T. Hodges, D. Jacquemart, V. I.

Perevalov, A. Perrin, K. P. Shine, M.-A. H. Smith, J. Tennyson, G. C. Toon, H. Tran, V. G. Tyuterev, A. Barbe, A. G. Császár, V. M. Devi, T. Furtenbacher, J. J. Harrison, J.-M. Hartmann, A. Jolly, T. J. Johnson, T. Karman, I. Kleiner, A. A. Kyuberis, J. Loos, O. M. Lyulin, S. T. Massie, S. N. Mikhailenko, N. Moazzen-Ahmadi, H. S. P. Müller, O. V. Naumenko, A. V. Nikitin, O. L. Polyansky, M. Rey, M. Rotger, S. W. Sharpe, K. Sung, E. Starikova, S. A. Tashkun, J. V. Auwera, G. Wagner, J. Wilzewski, P. Wcisło, S. Yu, E. J. Zak, The HITRAN2016 molecular spectroscopic database. *J. Quant. Spectrosc. Radiat. Transf.* **203**, 3–69 (2017).

23. L. S. Rothman, I. E. Gordon, A. Barbe, D. C. Benner, P. E. Bernath, M. Birk, V. Boudon, L. R. Brown, A. Campargue, J. P. Champion, K. Chance, L. H. Coudert, V. Dana, V. M. Devi, S. Fally, J. M. Flaud, R. R. Gamache, A. Goldman, D. Jacquemart, I. Kleiner, N. Lacome, W. J. Lafferty, J. Y. Mandin, S. T. Massie, S. N. Mikhailenko, C. E. Miller, N. Moazzen-Ahmadi, O. V. Naumenko, A. V. Nikitin, J. Orphal, V. I. Perevalov, A. Perrin, A. Predoi-Cross, C. P. Rinsland, M. Rotger, M. Simeckova, M. A. H. Smith, K. Sung, S. A. Tashkun, J. Tennyson, R. A. Toth, A. C. Vandaele, J. Vander Auwera, The HITRAN 2008 molecular spectroscopic database. *J. Quant. Spectrosc. Radiat. Transf.* **110**, 533–572 (2009).

24. S. M. McGinn, H. H. Janzen, T. W. Coates, K. A. Beauchemin, T. K. Flesch, Ammonia Emission from a Beef Cattle Feedlot and Its Local Dry Deposition and Re-Emission. *J. Environ. Qual.* **45**, 1178–1185 (2016).

25. "U.S. Standard Atmosphere, 1976" (U.S. Government Printing Office, Washington, D.C., 1976), (available at https://ntrs.nasa.gov/search.jsp?R=19770009539).

26. H. F. Bonifacio, R. G. Maghirang, E. B. Razote, S. L. Trabue, J. H. Prueger, Comparison of AERMOD and WindTrax dispersion models in determining PM10 emission rates from a beef cattle feedlot. *J. Air Waste Manag. Assoc.* **63**, 545–556 (2013).

27. T. Flesch, J. Wilson, L. Harper, B. Crenna, Estimating gas emissions from a farm with an inverse-dispersion technique. *Atmos. Environ.* **39**, 4863–4874 (2005).

28. T. K. Flesch, J. D. Wilson, L. A. Harper, B. P. Crenna, R. R. Sharpe, Deducing Ground-to-Air Emissions from Observed Trace Gas Concentrations: A Field Trial. *J. Appl. Meteorol.* **43**, 487–502 (2004).

29. P. Werle, R. Mücke, F. Slemr, The limits of signal averaging in atmospheric trace-gas monitoring by tunable diode-laser absorption spectroscopy (TDLAS). *Appl. Phys. B Photophysics Laser Chem.* **57**, 131–139 (1993).

30. Z. J. DeBruyn, C. Wagner-Riddle, A. VanderZaag, Assessment of Open-path Spectrometer Accuracy at Low Path-integrated Methane Concentrations. *Atmosphere*. **11**, 184 (2020).

31. A. Schliesser, M. Brehm, F. Keilmann, D. van der Weide, Frequency-comb infrared spectrometer for rapid, remote chemical sensing. *Opt. Express*. **13**, 9029–9038 (2005).

32. E. D. Thoma, R. C. Shores, E. L. Thompson, D. B. Harris, S. A. Thorneloe, R. M. Varma, R. A. Hashmonay, M. T. Modrak, D. F. Natschke, H. A. Gamble, Open-Path Tunable Diode Laser Absorption Spectroscopy for Acquisition of Fugitive Emission Flux Data. *J. Air Waste Manag. Assoc.* **55**, 658–668 (2005).

33. R. K. Cole, A. S. Makowiecki, N. Hoghooghi, G. B. Rieker, Baseline-free quantitative absorption spectroscopy based on cepstral analysis. *Opt. Express*. **27**, 37920 (2019).

34. C. B. Alden, S. C. Coburn, R. J. Wright, E. Baumann, K. Cossel, E. Perez, E. Hoenig, K. Prasad, I. Coddington, G. B. Rieker, Single-Blind Quantification of Natural Gas Leaks from 1 km Distance Using Frequency Combs. *Environ. Sci. Technol.* **53**, 2908–2917 (2019).

35. P. Prajapati, E. A. Santos, Measurements of methane emissions from a beef cattle feedlot using the eddy covariance technique. *Agric. For. Meteorol.* **232**, 349–358 (2017).

36. W. F. Kissinger, R. K. Koelsch, G. E. Erickson, T. J. Klopfenstein, Characteristics of Manure Harvested from Beef Cattle Feedlots. *Appl. Eng. Agric.* **23**, 357–365 (2007).

37. R. W. Todd, N. A. Cole, M. B. Rhoades, D. B. Parker, K. D. Casey, Daily, Monthly, Seasonal, and Annual Ammonia Emissions from Southern High Plains Cattle Feedyards. *J. Environ. Qual.* **40**, 1090–1095 (2011).

38. D. L. Bjorneberg, A. B. Leytem, D. T. Westermann, P. R. Griffiths, L. Shao, M. J. Pollard, Measurement of Atmospheric Ammonia, Methane, and Nitrous Oxide at a Concentrated Dairy Production Facility in Southern Idaho Using Open-Path FTIR Spectrometry. *Trans. ASABE*. **52**, 1749–1756 (2009).

39. S. M. McGinn, T. K. Flesch, Ammonia and greenhouse gas emissions at beef cattle feedlots in Alberta Canada. *Agric. For. Meteorol.* **258**, 43–49 (2018).

40. F. Montes, C. A. Rotz, H. Chaoui, Process Modeling of Ammonia Volatilization from Ammonium Solution and Manure Surfaces: A Review with Recommended Models. *Trans. ASABE*. **52**, 1707–1720 (2009).

41. J. D. Beuning, E. Pattey, G. Edwards, B. J. Van Heyst, Improved temporal resolution in process-based modelling of agricultural soil ammonia emissions. *Atmos. Environ.* **42**, 3253–3265 (2008).

42. N. J. Hutchings, S. G. Sommer, S. C. Jarvis, A model of ammonia volatilization from a grazing livestock farm. *Atmos. Environ.* **30**, 589–599 (1996).

43. S. J. Eilerman, J. Peischl, J. A. Neuman, T. B. Ryerson, K. C. Aikin, M. W. Holloway, M. A. Zondlo, L. M. Golston, D. Pan, C. Floerchinger, S. Herndon, Characterization of Ammonia, Methane, and Nitrous Oxide Emissions from Concentrated Animal Feeding Operations in Northeastern Colorado. *Environ. Sci. Technol.* **50**, 10885–10893 (2016).

44. L. M. Golston, D. Pan, K. Sun, L. Tao, M. A. Zondlo, S. J. Eilerman, J. Peischl, J. A. Neuman, C. Floerchinger, Variability of Ammonia and Methane Emissions from Animal Feeding Operations in Northeastern Colorado. *Environ. Sci. Technol.* **54**, 11015–11024 (2020).

45. X.-F. Yu, Y.-X. Zhang, Y.-C. Zou, H.-M. Zhao, X.-G. Lu, G.-P. Wang, Adsorption and Desorption of Ammonium in Wetland Soils Subject to Freeze-Thaw Cycles. *Pedosphere*. **21**, 251–258 (2011).

46. K. Voglmeier, M. Jocher, C. Häni, C. Ammann, Ammonia emission measurements of an intensively grazed pasture. *Biogeosciences*. **15**, 4593–4608 (2018).

47. J. M. Pedersen, A. Feilberg, J. N. Kamp, S. Hafner, T. Nyord, Ammonia emission measurement with an online wind tunnel system for evaluation of manure application techniques. *Atmos. Environ.* **230**, 117562 (2020).

48. J. R. Brandle, L. Hodges, X. H. Zhou, in *New Vistas in Agroforestry: A Compendium for 1st World Congress of Agroforestry, 2004*, P. K. R. Nair, M. R. Rao, L. E. Buck, Eds. (Springer Netherlands, Dordrecht, 2004; https://doi.org/10.1007/978-94-017-2424-1_5), *Advances in Agroforestry*, pp. 65–78.

49. L. Ortolano, Estimating air quality impacts. *Environ. Impact Assess. Rev.* **5**, 9–35 (1985).

50. D. M. Bailey, E. M. Adkins, J. H. Miller, An open-path tunable diode laser absorption spectrometer for detection of carbon dioxide at the Bonanza Creek Long-Term Ecological Research Site near Fairbanks, Alaska. *Appl. Phys. B*. **123**, 245 (2017).

51. M. Nikodem, G. Plant, D. Sonnenfroh, G. Wysocki, Open-path sensor for atmospheric methane based on chirped laser dispersion spectroscopy. *Appl. Phys. B*. **119**, 3–9 (2015).

52. C. E. Owensby, J. M. Ham, L. M. Auen, Fluxes of CO_2 From Grazed and Ungrazed Tallgrass Prairie. *Rangel. Ecol. Manag.* **59**, 111–127 (2006).

53. H. Guo, C. Herkommer, A. Billat, D. Grassani, C. Zhang, M. H. P. Pfeiffer, W. Weng, C.-S. Brès, T. J. Kippenberg, Mid-infrared frequency comb via coherent dispersive wave generation in silicon nitride nanophotonic waveguides. *Nat. Photonics*, 1 (2018).

54. E. Baumann, E. V. Hoenig, E. F. Perez, G. M. Colacion, F. R. Giorgetta, K. C. Cossel, G. Ycas, D. R. Carlson, D. D. Hickstein, K. Srinivasan, S. B. Papp, N. R. Newbury, I. Coddington, Dual-comb spectroscopy with tailored spectral broadening in Si_3N_4 nanophotonics. *Opt. Express*. **27**, 11869–11876 (2019).

55. G. Ycas, F. R. Giorgetta, E. Baumann, I. Coddington, D. Herman, S. A. Diddams, N. R. Newbury, High-coherence mid-infrared dual-comb spectroscopy spanning 2.6 to 5.2 µm. *Nat. Photonics*. **12**, 202–208 (2018).

56. H. Timmers, A. Kowligy, A. Lind, F. C. Cruz, N. Nader, M. Silfies, G. Ycas, T. K. Allison, P. G. Schunemann, S. B. Papp, S. A. Diddams, Molecular fingerprinting with bright, broadband infrared frequency combs. *Optica*. **5**, 727–732 (2018).

57. M. A. Abbas, Q. Pan, J. Mandon, S. M. Cristescu, F. J. M. Harren, A. Khodabakhsh, Time-resolved mid-infrared dual-comb spectroscopy. *Sci. Rep.* **9**, 1–9 (2019).

58. Z. Chen, T. W. Hänsch, N. Picqué, Mid-infrared feed-forward dual-comb spectroscopy. *Proc. Natl. Acad. Sci.* **116**, 3454–3459 (2019).

59. J. L. Klocke, M. Mangold, P. Allmendinger, A. Hugi, M. Geiser, P. Jouy, J. Faist, T. Kottke, Single-Shot Sub-microsecond Mid-infrared Spectroscopy on Protein Reactions with Quantum Cascade Laser Frequency Combs. *Anal. Chem.* **90**, 10494–10500 (2018).

60. A. V. Muraviev, V. O. Smolski, Z. E. Loparo, K. L. Vodopyanov, Massively parallel sensing of trace molecules and their isotopologues with broadband subharmonic mid-infrared frequency combs. *Nat. Photonics*. **12**, 209–214 (2018).

61. A. S. Kowligy, H. Timmers, A. J. Lind, U. Elu, F. C. Cruz, P. G. Schunemann, J. Biegert, S. A. Diddams, Infrared electric field sampled frequency comb spectroscopy. *Sci. Adv.* **5**, eaaw8794 (2019).

62. A. R. Ravishankara, J. S. Daniel, R. W. Portmann, Nitrous Oxide (N_2O): The Dominant Ozone-Depleting Substance Emitted in the 21st Century. *Science*. **326**, 123–125 (2009).

63. K. Butterbach-Bahl, E. M. Baggs, M. Dannenmann, R. Kiese, S. Zechmeister-Boltenstern, Nitrous oxide emissions from soils: how well do we understand the processes and their controls? *Philos. Trans. R. Soc. B Biol. Sci.* **368**, 20130122 (2013).

64. S. Fares, D. R. Gentner, J.-H. Park, E. Ormeno, J. Karlik, A. H. Goldstein, Biogenic emissions from Citrus species in California. *Atmos. Environ.* **45**, 4557–4568 (2011).

65. Z. Gao, R. L. Desjardins, T. K. Flesch, Assessment of the uncertainty of using an inverse-dispersion technique to measure methane emissions from animals in a barn and in a small pen. *Atmos. Environ.* **44**, 3128–3134 (2010).

66. Z. Loh, D. Chen, M. Bai, T. Naylor, D. Griffith, J. Hill, T. Denmead, S. McGinn, R. Edis, Measurement of greenhouse gas emissions from Australian feedlot beef production using open-path spectroscopy and atmospheric dispersion modelling. *Aust. J. Exp. Agric.* **48**, 244 (2008).

67. M. C. McBain, R. L. Desjardins, The evaluation of a backward Lagrangian stochastic (bLS) model to estimate greenhouse gas emissions from agricultural sources using a synthetic tracer source. *Agric. For. Meteorol.* **135**, 61–72 (2005).

68. R. W. Todd, M. B. Altman, N. A. Cole, H. M. Waldrip, Methane Emissions from a Beef Cattle Feedyard during Winter and Summer on the Southern High Plains of Texas. *J. Environ. Qual.* **43**, 1125–1130 (2014).

69. S. P. Burns, T. W. Horst, L. Jacobsen, P. D. Blanken, R. K. Monson, Using sonic anemometer temperature to measure sensible heat flux in strong winds. *Atmos. Meas. Tech*. **5**, 2095–2111 (2012).

70. T. K. Flesch, V. S. Baron, J. D. Wilson, D. W. T. Griffith, J. A. Basarab, P. J. Carlson, Agricultural gas emissions during the spring thaw: Applying a new measurement technique. *Agric. For. Meteorol.* **221**, 111–121 (2016).

Acknowledgements

This work was partially funded by the NSF Division of Biological Infrastructure Award #1726304, the ARPA-E MONITOR program, the William and Joan Porter Endowment, and the Habiger Heritage Fund. The authors would like to acknowledge initial constructive discussions with Amit Chakrabarti, Ernest Minton, and Kristan Corwin. We

would like to thank Dale Blasi and William Hollenbeck for granting access to the Kansas State University Beef Stocker Unit. The authors also thank Jacob Friedlein and Nazanin Hoghooghi for useful comments on the manuscript. Use of manufacturers' or product names should not be construed as an endorsement.

Figures and Tables

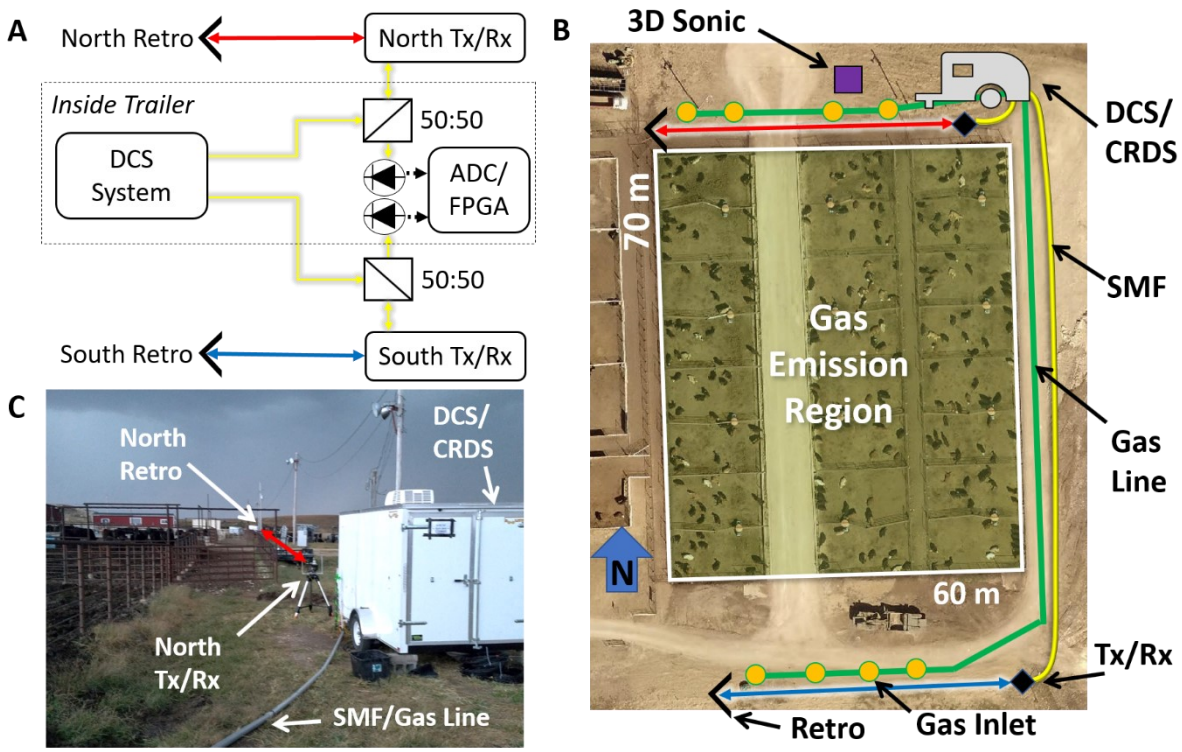

Fig. 1. Experimental setup. (A) Schematic of the dual-comb spectrometer for feedlot gas concentration measurements on two optical paths. Yellow lines indicate single-mode fiber (SMF) transmitting and receiving dual-comb light from the north (red arrow) and south (blue arrow) open-air paths. Note: display 50:50 beam splitters were fiber based. ADC/FPGA: analog-to-digital converter and field-programmable gate array. **(B)** Aerial image of Manhattan, Kansas feedlot. Approximation location of the trailer (gray) containing DCS and CRDS systems is marked as well as that of the 3D sonic anemometer (purple square), transmitting/receiving telescope (Tx/Rx; black diamonds), retroreflectors (black chevrons), gas inlets for the CRDS system (orange circles) and sampling gas line (green lines), north open-air path (red arrow), south open-air path (blue arrow) and SMF for dual-comb transport (yellow lines). The gas emission region only included the animal pens with an area of 3731 m^2. **(C)** Photograph of the north end of the site including the trailer housing both DCS and CRDS systems, the PVC tubing for south path SMF and gas line, Tx/Rx for the north path and the north path retroreflector.

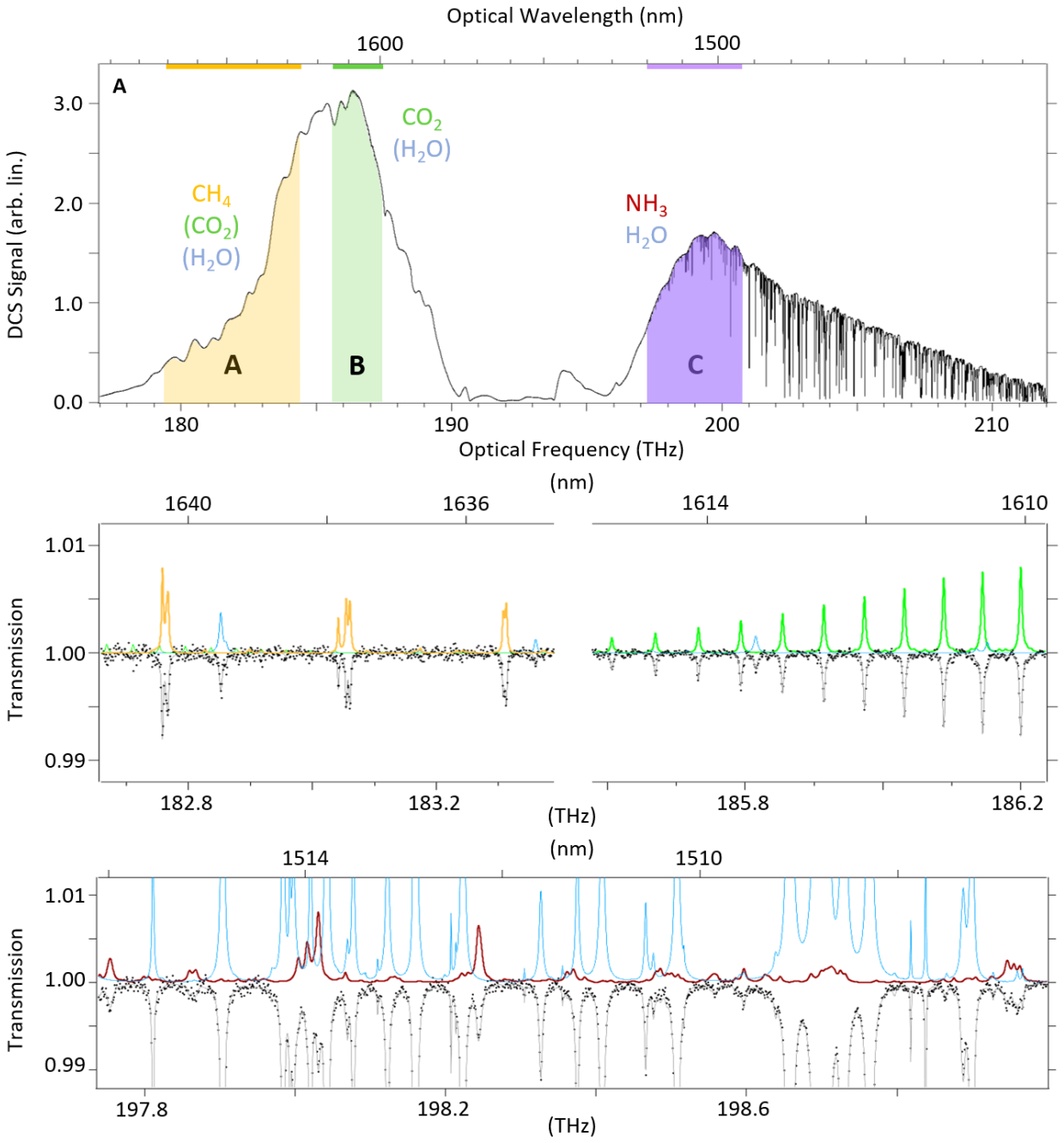

Fig. 2. Broadband, high resolution DCS spectra taken at the downwind edge of the feedlot. (A) Full DCS spectrum at 5-minute averaging time with highlighted sections showing the three spectral bands of interest (1, 2 and 3). Absorbing molecules are indicated each band with weak, interfering species shown in parentheses. **(B)** Example sub-section of band 1. DCS data is shown in black with a fit to a HITRAN model in gray. The inverted axis shows transmission models for each individual species – CH_4 in yellow, H_2O in blue, CO_2 in green and NH_3 in maroon. **(C)** Example sub-section of band 2 with CO_2 and weak H_2O. **(D)** A sub-section of band 3 highlighting the benefit of high resolution and large bandwidth, allowing retrieval of weak NH_3 in a strong interfering H_2O background. Note that while DCS data in B to D are down-sampled to 1 GHz resolution for clear visualization, all fitting is done at the native resolution (200 MHz). Models shown here are for a 100 m round-trip path and 3.04 ppm CH_4, 452 ppm CO_2, 0.57% H_2O, and 1.23 ppm NH_3.

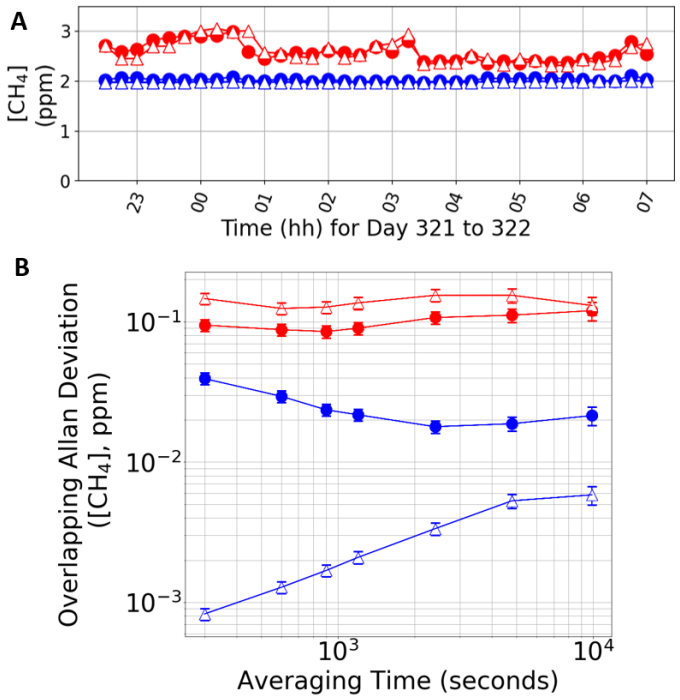

Fig. 3. Upwind and downwind CH_4 concentrations and associated instabilities. (A) Time series of DCS (closed circle) and CRDS (open triangles) measured north (red) and south (blue) dry concentrations of CH_4. **(B)** Allan-Werle analysis of CH_4 concentrations calculated using all data displayed in the above time series; Upwind DCS (blue circles), downwind DCS (red circles), upwind CRDS (blue triangle), downwind CRDS (red triangles). Note that the instability of the upwind concentrations is lower for the CRDS. For the downwind case, the DCS data shows lower instability.

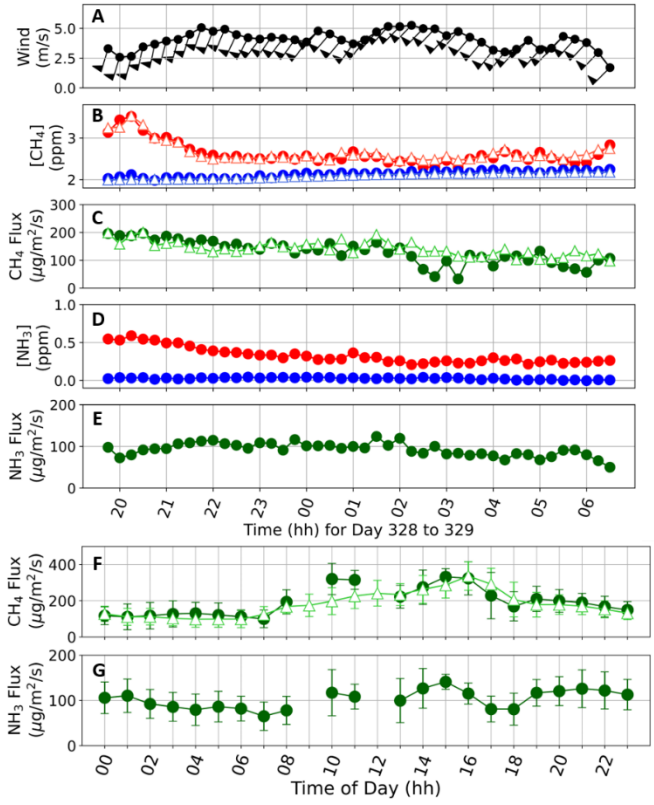

Fig. 4. Time-resolved CH_4 and NH_3 flux and averaged hourly diurnal flux cycles. Example data set covering an 11-hour period showing **(A)** wind conditions at the measurement site, **(B)** CH_4 concentrations (averaged to 15 minute time resolution) retrieved from the DCS (solid circles) and CRDS (open triangles) systems for north (red) and south (blue) paths, **(C)** the corresponding methane flux retrieved from these DCS and CRDS measurements, **(D)** NH_3 concentrations from the DCS system and **(E)** the corresponding ammonia flux. The wind barbs point to the direction from which the wind is coming. **(F)** Diurnal cycle of CH_4 flux determined by DCS (solid circles) and CRDS (open triangles) when cattle were at the site (October 2019 to December 2019). Error bars are calculated by taking the standard deviation of all 15-minute averages included in each time bin. The increase in CH_4 flux between hours 8 and 16 is due to increased enteric fermentation after cattle feeding. **(G)** Diurnal cycle of NH_3 flux determined by DCS.

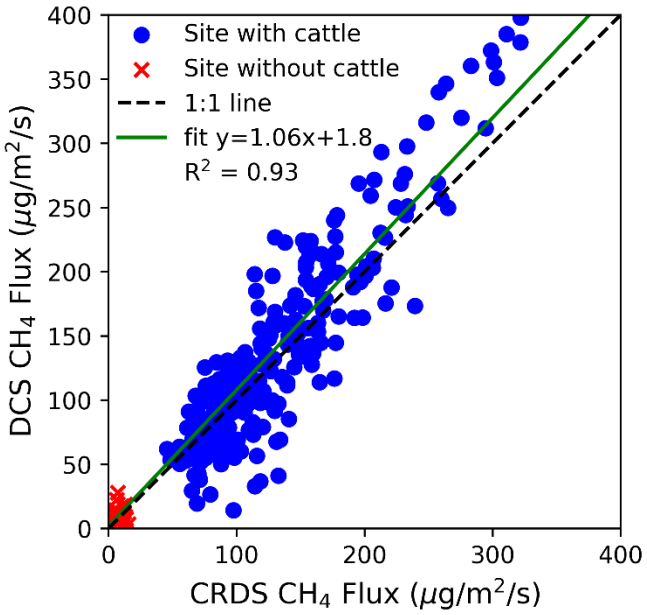

Fig. 5. Correlation between DCS and CRDS CH_4 flux. The data is fit to a line, determining the vertical intercept using fluxes without cattle (red x) and the slope was determined using all data. This process demonstrates 6% overall agreement between the DCS and CRDS CH_4 flux with a background offset of ~2 $\mu g/m^2/s$ (~2% of usual flux with cattle present).

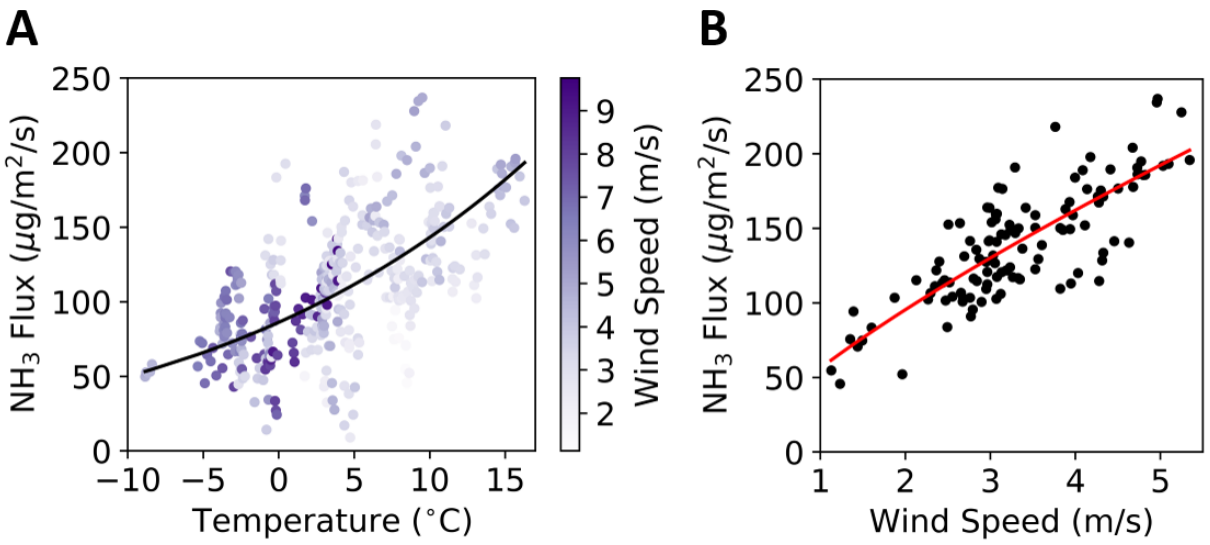

Fig. 6. Dependence of NH_3 emission rate on environmental parameters. **(A)** NH_3 flux (15-minute averages) versus ambient air temperature. Color indicates 15-minute averaged wind speed (U) for given flux estimate. Black line represents fit ($R^2 = 0.36$) to functional form for Henry's volatility constant (*40*). Note the large deviations of flux values near 0 °C corresponding to complicated dynamics associated with freeze-thaw cycles. **(B)** NH_3 flux (15-minute averages; black dots) versus U for ambient air temperature greater than 7°C. Red line represents fit ($R^2 = 0.65$) to power law $F = AU^B$ with $A = 56.1$ μg/m^2/s and $B = 0.77$.

Author Contributions

D.I.H., N.R.N., S.M.W., B.D.D., I.C., E.A.S. and B.R.W. conceived of and designed the experiments. D.I.H., G.M.C., I.C. and B.R.W built the DCS system. D.I.H., C.W., L.C.H., E.A.S. and B.R.W. performed the experiments. D.I.H., F.R.G., I.C. and B.R.W. analyzed the DCS data. C.W. and E.A.S. analyzed the CRDS data. B.R.W, E.A.S., D.I.H. and I.C. implemented the inverse dispersion model. B.R.W., D.I.H., I.C., E.A.S., K.C.C and E.M.W. analyzed the flux data. D.I.H, B.R.W., I.C. and E.A.S. wrote the manuscript. B.R.W. and E.A.S. supervised the project.

Competing Interests

The authors declare no competing financial interests.

Supplementary Materials

Feedlot Weather Conditions

Wind conditions and temperature at the feedlot (Lat. 39.237˚ W, Long. 96.636˚ N) were measured continuously for 59 days (Day 303 to Day 362) using a 3D sonic anemometer (CSAT3, Campbell Sci.). Wind speed and direction are displayed as a windrose (fig. S1A). A windrose shows the frequency of winds blowing from the sixteen cardinal directions with radial 'spokes' that are binned directions (each 22.5˚ wide) and with concentric 'rings' that represent a percentage of time. The six spoke colors, as shown in the legend, are binned wind speeds in m/s. Northerly and southerly winds were more frequent at the site as indicated by the longer length spokes in the ($315^\circ < \theta < 45^\circ$) and ($135^\circ < \theta < 225^\circ$) regions. The sonic anemometer recorded the temperature at the site and precipitation was recorded at a nearby weather station in Manhattan, KS (KState Mesonet MTNK1) located at Lat. 39.209˚ W, Long. 96.552˚ N (fig. S1B). While the accumulated rainfall during the measurement was only 10.7 mm, the ground at the site was initially very wet from the 61.0 mm accumulated rainfall in October 2019.

DCS/CRDS Methane Concentration Correlations

Linear correlation is observed between DCS and CRDS concentration measurements on both the north and south open-air paths (fig. S3). A one-to-one correlation indicates exact agreement between the two sensors and validates our wind condition criteria. The north and south path data were fit to lines and exhibited respective slopes of 0.94±0.01 and 1.10±0.01 with coefficients of determination (R^2) above 0.9. As the measurement paths were not perfectly

symmetric in their location relative to the cattle pen and measurement trailer, it is not surprising that these slopes differ from one asymmetrically. DCS concentrations were greater than CRDS on the north path and vice versa on the south path. Still both slopes indicate CH_4 concentration measurements using DCS and CRDS agree safely at the sub 10% level. At the background level of ~2 ppm, the fitted lines showed offsets of ≤ 20 ppb on both paths, demonstrating good overall agreement between DCS and CRDS upwind CH_4 measurements.

Water and Carbon Dioxide Concentrations

The DCS also captures absorption from water vapor and carbon dioxide emitted by the feedlot system. Time dependent DCS and CRDS concentration enhancements for both species match closely (fig. S2, A and B). Here, a 4% multiplier was included in the DCS water data (fig. S2A) with some of this offset likely coming from errors in HITRAN 2008 line-strengths and temperature dependences (*23*). Considering that 100 ppm enhancements of H_2O were typical for our measurement conditions, a ~5% level uncertainty in absolute water concentrations (nominally about 250 ppm) makes water flux estimation difficult. Although the absolute concentrations do not agree between the sensors, H_2O enhancements measured by DCS and CRDS generally agree to within 30 ppb (~15% of total enhancement). In previous studies, attenuation of water vapor due to adsorption in tubing systems was observed (*35*), further complicating the comparison of DCS and CRDS data in this work. For future agricultural water vapor measurements, in-depth studies of water spectral temperature dependences, line-strengths and lineshapes will be required for accurate measurement over kilometer scale agricultural systems. Here, the absolute error in the H_2O concentration is not large enough to affect the calculation of dry air CH_4 and NH_3 concentrations.

Although CO_2 is the most significant anthropogenic greenhouse gas (GHG), animal agriculture is not a leading source of CO_2 compared to other economic sectors such as transportation or manufacturing (*1*). However, in animal grazing systems, it is important to monitor CO_2 flux in order to understand limits on soil carbon uptake (*52*). Unlike CH_4, in a feedlot setting, the concentration enhancements of CO_2 are only ~5% of the background level. Also, despite the large atmospheric background CO_2 levels (415 ppm) of the atmosphere, near-infrared (NIR) cross-sections of CO_2 are quite weak, making quantification of CO_2 difficult with this comb source over a short path length. CO_2 flux estimation was possible only when DCS figure-of-merit (FOM) was large as explained below.

A large time-dependent CO_2 concentration enhancement was recorded on the night of 11/16/2019 with both DCS and CRDS data coverage over the north and south paths (fig. S2B). Due to differences in telescope alignment, the north path FOM on 11/16/2019 was 10^7 whereas the south path FOM was 6.5×10^6 with the slightly higher noise levels

evident on the background CO_2 data. During ideal measurement conditions with DCS FOM near 8×10^6 (*i.e.* with ~150 μW of power coupled onto the detector), the background Allan-Werle deviation at 900 seconds is calculated to be 1.8 ppm (90 ppm·m), comparable to precision of open-path CW lasers reported in the literature (*50*). This path-normalized Allan-Werle deviation is about two times smaller than the path-normalized sensitivity reported in previous DCS demonstrations (*15*). In these optimal conditions, CO_2 flux measurement was possible, however, if the DCS FOM dropped to 3×10^6 or below, the DCS CO_2 uncertainty would exceed 5 ppm, making accurate flux analysis difficult for many datasets since CO_2 enhancements generally hovered around 15 to 20 ppm. Additionally, due to its spectral position near the DCS peak signal, the CO_2 fits saw increased baseline noise due to drifts in the supercontinuum spectrum and other chromatic effects in the optical system. In order to provide increased signal-to-noise ratio (SNR), it will be necessary to measure CO_2 absorption in other bands, namely the 2.1 μm, 4.2 μm or 4.7 μm bands (*54*, *55*). The CO_2 absorption in these regions is between 10× to 1000× stronger than the absorption in the NIR. With a DCS measurement in one of these more sensitive regions, it should be possible to reach CO_2 precisions of less than 0.1 ppm in 1000 seconds, which would be necessary to characterize the single ppm level enhancements expected in the context of a grazing system.

Spectroscopic Bias in CH_4 and NH_3 Emission Estimates

For concentration retrievals reported in this paper, the temperature used for cepstral fitting was fixed to the value provided by the sonic anemometer. The pressure was fixed to the value provided by the on-site weather station. By changing the input temperature in the fitting code, the absolute CH_4 concentrations was found to be slightly biased at the level of ~10 ppb/K. This temperature effect is common to the upwind and downwind paths up to ~0.35% of the absolute CH_4 per K. Temperature can also be extracted from the cepstral fits for band C, predominantly from the strong water absorption signal. Temperatures received from fitting to HITRAN models were within 4 K of the sonic anemometer value. This 4 K offset is larger than temperature uncertainty effects due to humidity (*69*) and vertical gradients between the laser paths and the sonic anemometer (*70*), which should both be on the order of 1 K or less. Thus, taking this 4 K offset as our temperature uncertainty leads to a conservative methane flux uncertainty of 1.5% due to temperature effects. Errors in the modeled pressure also mostly lead to common-mode effects on the two paths and a negligible effect on the reported flux. Significant water clutter in band C (Fig. 2D) slightly complicates the temperature bias for the absolute NH_3 concentrations. Interference with H_2O should also affect wavelength modulation spectroscopy systems operating in the same band (*32*) as H_2O levels in the atmosphere can change dramatically. By

again manually adjusting the fit temperature, the downwind ammonia bias was estimated at between 0.75% to 1% of the absolute concentration per K (i.e. ~4 ppb/K for the average enhancement). Even though the upwind ammonia concentration is close to zero, crosstalk in the fitting regression causes a slight ammonia bias of ~3 ppb/K for nominal atmospheric water vapor levels. Removing the common-mode portion of ammonia temperature bias on the two paths leaves a residual flux bias of ~0.4%/K. Thus, the ammonia flux reported in this work has approximately 1.5% uncertainty due to temperature effects. Simulation of the band C spectra also demonstrated that the cepstral fitting procedure has high immunity to errors in the modeled pressure (~100 ppt/hPa). An Allan-Werle analysis was also performed on the difference between the north and south DCS-retrieved temperature time series from 11/16/2019. This analysis showed precision of 0.07 K at 900 seconds or about 15% of the temperature difference of 0.5 K. This high sensitivity to differences in path-averaged temperatures could enable precise agricultural heat flux measurements.

As discussed in the main text, there are also small biases due to cepstral filter choice and detector nonlinearity, both at the <5% level. In total, the ammonia flux systematic biases discussed here are below 10%, an improvement over 20% level uncertainty normally attributed to modern ammonia sensing technologies (*8*, *9*, *43*). It is worthwhile to note that an Allan-Werle analysis of NH_3 background concentrations averages down to the 2 ppb (100 ppb·m) level at 10^4 seconds for the night of 11/17/2019. The ability to average for this amount of time without drifts is a problem for commercial NH_3 open-path sensors (*8*), possibly due to unaccounted interference from neighboring water absorption lines.

Supplementary Figures

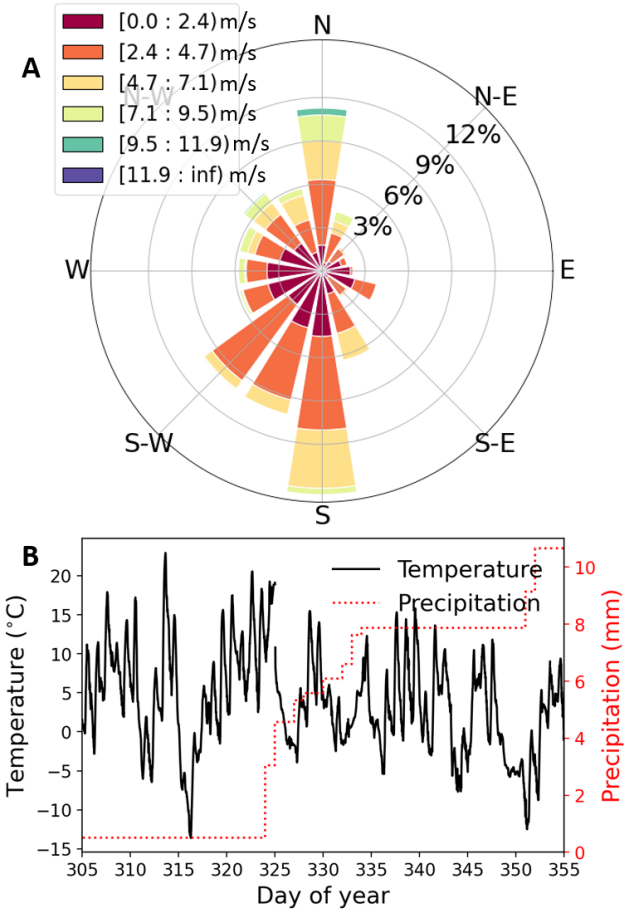

fig. S1. Weather conditions at the feedlot during measurement campaign. (A) Windrose showing the frequency of wind speed and direction at the site. The legend shows wind speed bins in m/s. **(B)** Measured 15-minute averaged temperature and accumulated daily precipitation.

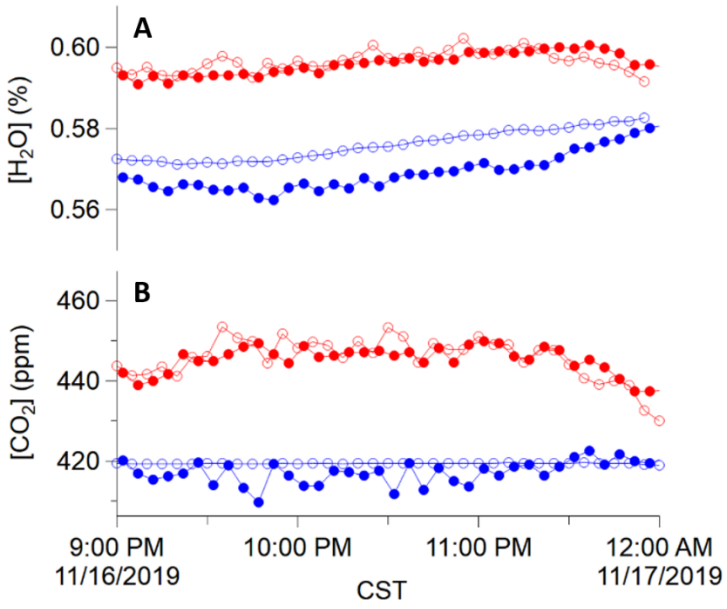

fig. S2. H_2O and CO_2 enhancements measured by DCS and CRDS. (A) H_2O concentrations for late hours on 11/16/2019. Red dots indicate north path 5-minute averages. Blue dots indicate south path 5-minute averages. Opaque (hollow) dots indicate DCS (CRDS) data. The DCS data has been multiplied by 1.04 for comparison against the CRDS data. **(B)** CO_2 concentrations from the same time period and sensors.

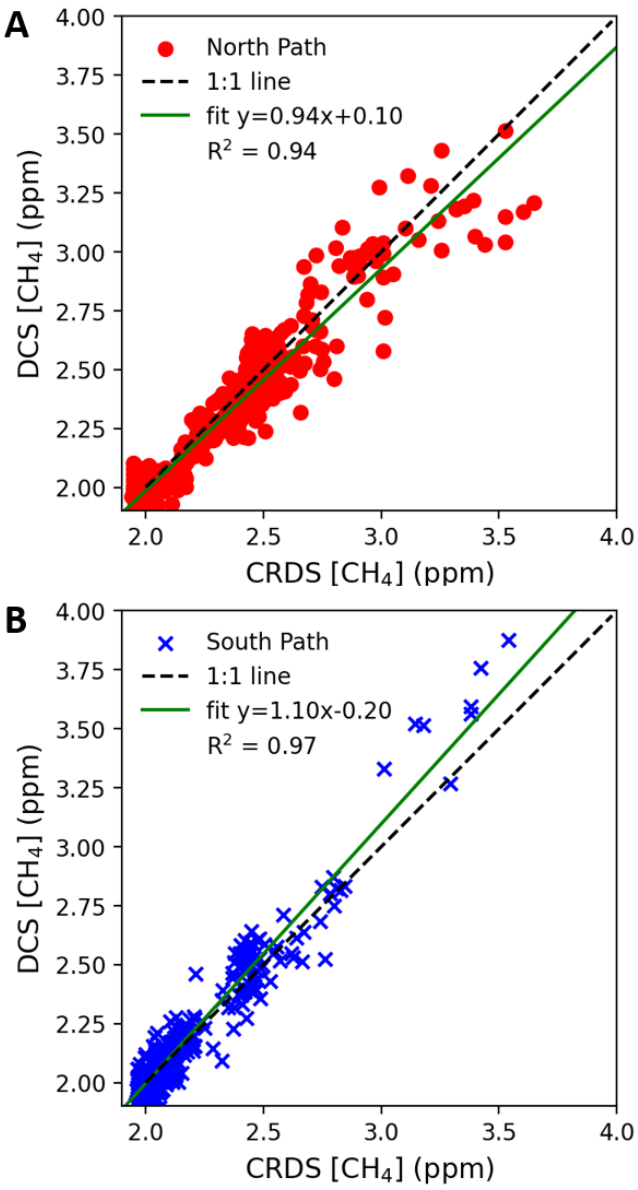

fig. S3. **Direct comparison of CH_4 concentrations measured by DCS and CRDS.** Correlation between DCS and CRDS measured CH_4 concentrations (including all time periods) measured along the **a,** north path and **b,** south path. A close agreement between north sensors of 6% is demonstrated by the slope of the correlation plot. At background levels (2 ppm), the agreement is 20 ppb (1% of background). The south path has overall agreement to within 10% and background agreement at the ppb level.